

Deep Needlet: A CNN based full sky component separation method in Needlet space

Debabrata Adak^{1,2,3,4}

¹Instituto de Astrofísica de Canarias, E-38200 La Laguna, Tenerife, Spain

²Departamento de Astrofísica, Universidad de La Laguna, E-38206 La Laguna, Tenerife, Spain

³The Institute of Mathematical Sciences, CIT Campus, Chennai 600113, India

⁴Homi Bhabha National Institute, Training School Complex, Anushakti Nagar, Mumbai 400085, India

E-mail: adak@iac.es

Abstract. One of the most important steps of Cosmic Microwave Background (CMB) data analysis is component separation to recover CMB map by combining the observations contaminated by foregrounds. Needlet Internal Linear Combination (NILC) is one of the successful methods that applies the minimum variance estimation technique to a set of needlet-filtered frequency maps to recover CMB. This work develops a deep convolutional neural network (CNN) model to recover CMB map from needlet-filtered frequency maps over the full sky. The model allows to perform component separation with a multi-resolution representation of spherical data localized on both pixel space and harmonic space with rotational invariant features of CMB. The network model is trained on realistic simulations at *Planck* frequencies. We demonstrate the network performance for simulations that exhibit different foreground complexities. The model achieves precise recovery of the CMB temperature map and the TT power spectrum exhibits excellent agreement with true value up to $\ell \sim 1100$. The residual leakage to the recovered CMB is reduced significantly compared to the CMB map recovered using NILC pipeline. Once validated on the simulations, the network is applied to *Planck* PR3 data to recover CMB. The recovered CMB map shows excellent agreement with CMB maps of *Planck* legacy products using NILC and SMICA pipelines. This work demonstrates a powerful component separation method to clean spherical signal data from multi-resolution wavelet-filtered maps.

Contents

1	Introduction	1
2	Needlet ILC method	2
3	CNN architecture	4
4	Data	6
4.1	simulations	6
4.2	Planck data	7
5	data processing	7
6	Model training and CMB recovery	7
6.1	Testing the impact of dust complexity	11
6.2	Dependency on choice of frequency channels	13
7	Application to <i>Planck</i> data	13
8	Discussion and Summary	15
9	Acknowledgment	15
A	Dependency on instrument noise	16

1 Introduction

The cosmic microwave background (CMB) anisotropy is the snapshot of the Universe after epoch of recombination. The map contains a tons of information about early and late Universe which is seen to be a crucial pillar in study of cosmology. The temperature anisotropy of CMB in addition to CMB polarization data are proven to be extremely useful to build the concordance model of the Universe. Therefore ground-based, balloon-borne and satellite missions are being designed, planed and operated to observe the sky at millimeter (mm) and sub-millimeter (submm) bands [1–11]. However, we can only observe the CMB through Galactic and extragalactic contamination of thermal dust, synchrotron, anomalous microwave emission (AME), free-free, CO, Cosmic Infrared Background (CIB) and Sunyaev–Zeldovich (SZ) effects (see [12] for review). Therefore, component separation methods play a critical role to recover CMB maps from foreground contaminated data. Since last decades many component separation algorithms have been developed to clean the CMB using multi-frequency observations [13–22]. Some of these algorithms are blind that does not assume any particular model of foreground emissions [13, 14]. Some methods are parametric [15, 23] and some works at interface of both [20–22]. The main motivation of developing different algorithms is to reduce residual leakage of foregrounds and instrument noise to recovered CMB map.

Needlet Internal Linear combination (NILC) method is one of the successful methods extensively applied to *Planck* and WMAP data analysis [24]. It is designed to improve the performance of Internal Linear combination (ILC, [13]). The methods exploit the fact that foregrounds follow different spectra other than CMB and uncorrelated to CMB anisotropy. The Galactic foregrounds are dominant at large angular scales. On the other hand instrument noise and extragalactic components are crucial contaminants at small angular scales. The needlet is a type of wavelet that enjoys localization in both pixel domain and harmonic space. Therefore minimum variance technique on needlet-filtered maps performs better than pixel/harmonic space ILC methods [13, 25]. However, the uncertainties in CMB calibration, loss of information at large scales for cut-sky data and any chance correlation between CMB and other components introduce bias in this method [16, 26].

Foregrounds are non-Gaussian and anisotropic in nature. Therefore, minimum variance estimation technique perhaps is non-optimal in the presence of higher-order statistics introduced by foregrounds. Therefore an artificial neural network can be helpful since the method can approximate arbitrary functions with trainable hyper-parameters and nonlinear transformations [27]. The deep convolutional neural networks (CNN) are found to have excellent performance in image recognition and classification problems. An extensive application of the technique in different machine learning (ML) models is seen in cosmological data analysis including CMB [28–43]. The cosmological application of neural network demands the network architecture should not encode either direction or position according to cosmological principle. In particular, for application of CNN for CMB data analysis, CNN should be efficient to maintain rotational invariance on \mathbb{S}^2 [44]. Therefore several CNN techniques are developed to perform convolution over spherical data [45–49]. In particular, a full sky component separation algorithm is developed in [50] using DeepSphere algorithm [49]. The method is found to be sub-optimal at angular scales of $\ell > 900$. More recently [51] applies the U-Net model [52] approximating the HEALPix maps on \mathbb{S}^2 to \mathbb{R}^2 plane of size $4N_{\text{side}} \times 3N_{\text{side}}$. The method achieves excellent success in the agreement between recovered power spectrum and the ground truth at $\ell < 900$. In this work, we develop a network model to apply to needlet-filtered frequency data at mm and submm bands to perform component separation. This work proposes to test the possible improvement that can be achieved by working on multi-resolution needlet-filtered maps. Instead of providing the full Fourier information of the data in a single set of training images, in this work, we employ the multiple band-filtered images to CNN model. This helps the network to train the non-Gaussian features of foregrounds at different scales and therefore more adequate subtraction of foregrounds.

We develop a U-Net architecture, a feedforward neural network model that has been inspired by neuroscience image classification in [52] and previous works on component separation [42, 50, 51]. The details of the network architecture are discussed in Section 3. We adopt the concept of Wang et al. [51] to approximate HEALPix maps to \mathbb{R}^2 plane of size $4N_{\text{side}} \times 3N_{\text{side}}$ that can help easy application of CNN on \mathbb{R}^2 and approximately preserve the rotational invariance of the spherical data.

The paper is organized as follows. We discuss the needlet decomposition of the maps and NILC minimum variance estimation technique in Section 2. In Section 3 we discuss the CNN model, namely **Deep Needlet** developed in this work. The foreground models used in network training and testing and *Planck* data are described in Section 4. The data used in the input and output layers of the model is preprocessed for easy application of CNN which is described in Section 5. Section 6 discusses the training procedure of the network and test results on different foreground complexities and frequency configurations. The application of the network model to *Planck* data and corresponding results are discussed in Section 7. Finally, we summarise the main findings of this work in Section 8. In Appendix A, we discuss the bias in the recovered CMB map in more detail.

2 Needlet ILC method

In this section, we discuss the methodology of CMB recovery using NILC pipeline. CMB observations provide frequency maps convolved with beam FWHM at respective channels. In harmonic space the observed frequency maps can be written as

$$X_{\ell m, \nu}^{Obs} = a_{\nu} b_{\ell, \nu} X_{\ell m}^{CMB} + b_{\ell, \nu} X_{\ell m}^{FG} + X_{\ell m, \nu}^{Noise}, \quad (2.1)$$

where a_{ν} is the CMB calibration coefficient and $b_{\ell, \nu}$ is the beam transfer function at frequency ν . In thermodynamic unit $a_{\nu} = 1$ up to the calibration uncertainty. The $X_{\ell m}^{CMB}$, $X_{\ell m}^{FG}$ and $X_{\ell m}^{Noise}$ are the harmonic coefficients of CMB, total foregrounds and instrument noise respectively.

All the frequency maps are first deconvolved with respective beam FWHM and convolved with a common beam transfer function b_{ℓ}^c ,

$$X_{\ell m, \nu} = \frac{b_{\ell}^c}{b_{\ell, \nu}} X_{\ell m, \nu}^{Obs}. \quad (2.2)$$

Table 1: List of needlet bands used in the analysis.

Band index	l_{min}	l_{peak}	l_{max}	Nside
1	0	0	50	32
2	0	50	100	64
3	50	100	150	128
4	100	150	250	128
5	150	250	350	256
6	250	350	550	512
7	350	550	650	512
8	550	650	800	512
9	650	800	1100	1024
10	800	1100	1500	1024
11	1100	1500	1800	1024

We choose $\text{FWHM} = 7.27'$ to be the common beam resolution. All maps are then decomposed into a set of filtered maps $\beta_j(\hat{n})$ applying a spherical needlet defined as,

$$\psi_{jk}(\hat{n}) = \sqrt{\lambda_{jk}} \sum_{\ell=0}^{\ell_{max}} \sum_{m=-\ell}^{\ell} h_{\ell}^j Y_{\ell m}^*(\hat{n}) Y_{\ell m}(\hat{\xi}_{jk}), \quad (2.3)$$

where the needlet filters h_{ℓ}^j are localised in the harmonic space that preserves the relation:

$$\sum_j h_{\ell}^j = 1. \quad (2.4)$$

The λ_{jk} s are the cubature weights corresponding to the choice of **Nside** suitable for j th needlet band. In practice the needlet coefficient maps are obtained by filtering the harmonic coefficients $X_{\ell m, \nu}$ with filter function h_{ℓ}^j as,

$$\beta_{j, \nu}(\hat{n}) = \sum_{\ell, m} h_{\ell}^j X_{\ell m, \nu} Y_{\ell m}(\hat{n}). \quad (2.5)$$

In this project, we design the needlet filters as follows:

$$h_{\ell}^j = \begin{cases} \cos \left[\left(\frac{\ell_{peak}^j - \ell}{\ell_{peak}^j - \ell_{min}^j} \right) \frac{\pi}{2} \right] & \text{for } \ell_{min}^j \leq \ell < \ell_{peak}^j \\ 1 & \text{for } \ell = \ell_{peak}^j \\ \cos \left[\left(\frac{\ell - \ell_{peak}^j}{\ell_{max}^j - \ell_{peak}^j} \right) \frac{\pi}{2} \right] & \text{for } \ell_{peak}^j < \ell \leq \ell_{max}^j. \end{cases} \quad (2.6)$$

The $\ell_{max}^j, \ell_{min}^j, \ell_{peak}^j$ and resolution of **HEALPix** grid for projecting needlet coefficient maps for different bands are listed in Table 1. The band shapes of filter functions are shown in Figure 1. The needlet coefficients are computed on **HEALPix** grids having suitable resolution parameter **Nside** equal to the smallest power of 2 larger than $\ell_{max}^j/2$.

At each needlet bands all frequency maps are linearly combined by weights w_{ν}^j to get minimum variance estimated CMB needlet coefficient maps,

$$\hat{\beta}_j^{NILC}(\hat{n}) = \sum_{\nu} w_{\nu}^j(\hat{n}) \beta_{j, \nu}(\hat{n}), \quad (2.7)$$

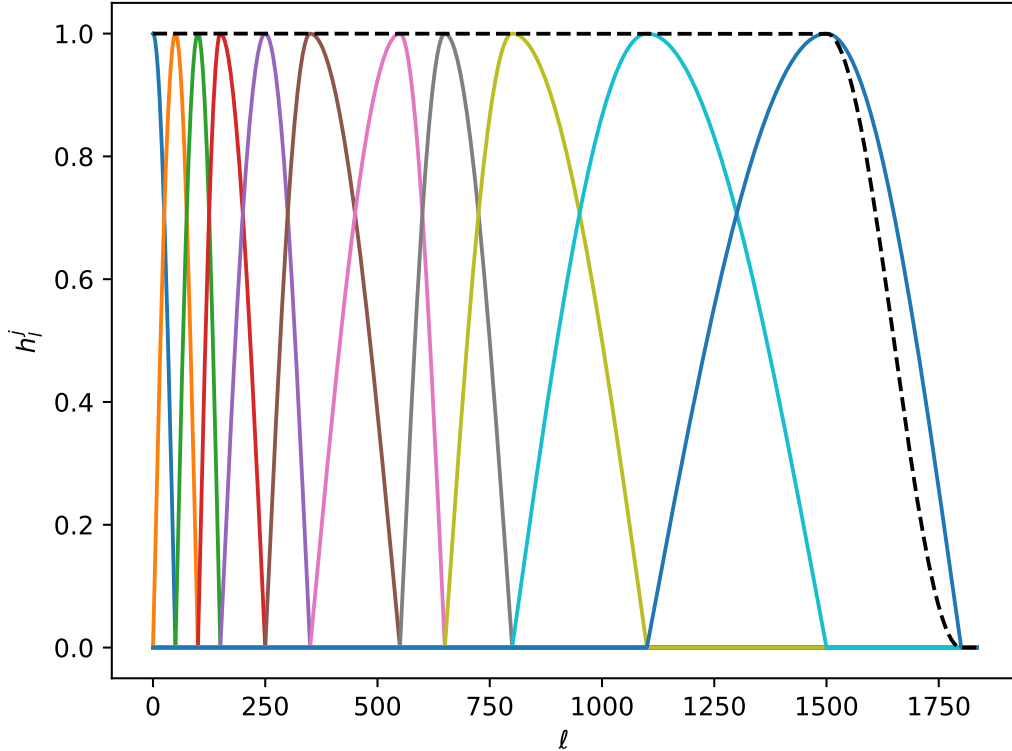


Figure 1: The band shapes of needlet filters designed in Table 1. The black dashed line displays normalisation of the needlet bands, i.e. the total filter applied in needlet decomposition of the map.

where the weights at each pixel are computed from the band covariance matrix, $C_{\nu,\nu'}^j(\hat{n}) = \langle \beta_{j,\nu}(\hat{n})\beta_{j,\nu'}(\hat{n})W_j^{PIX}(\hat{n}) \rangle$ as,

$$w_{\nu}^j(\hat{n}) = \frac{\sum_{\nu'} [C_{\nu,\nu'}^j(\hat{n})]^{-1}}{\sum_{\nu,\nu'} [C_{\nu,\nu'}^j(\hat{n})]^{-1}}. \quad (2.8)$$

The window function $W_j^{PIX}(\hat{n})$ defines the domain over which the covariance is computed and this is a Gaussian smoothing function in pixel domain having different beam width at different band depending on independent modes at corresponding needlet band [53]. The final NILC CMB map is then reconstructed by inverse filtering $\hat{\beta}_j^{NILC}(\hat{n})$ with same filters with h_{ℓ}^j used in decomposition of frequency maps following,

$$\hat{X}^{CMB}(\hat{n}) = \sum_{\ell m} \sum_j (\hat{\beta}_j^{NILC}(\hat{n})h_{\ell}^j)Y_{\ell m}^*(\hat{n}). \quad (2.9)$$

The final recovered map $\hat{X}^{CMB}(\hat{n})$ contains true CMB along with some contamination from foreground and noise residuals.

3 CNN architecture

The fundamental building block of a feedforward neural network is a model to map a set of images $\mathbf{X} = \{X_1, X_2, \dots, X_n\}$ to final output image $f_{w,b}(\mathbf{X}) \simeq Y$ with a set of trainable hyperparameters $\{w, b\}$

Table 2: The U-Net architecture used in this work for input and output maps of $\text{Nside}=1024$. A similar version of same architecture at different Nsides are used at different Needlet bands based on their respective resolution. Output size of maps at different hidden layers are written in third and fifth columns. The third quantities in output layer shapes are number of filters applied to corresponding convolution. The corresponding Nsides of input/output maps are listed in left most column.

Nside	Encoder block		Decoder block	
	Layers	Output layer shape	Layers	Output layer shape
1024	Conv2D block (c_1)	(2048, 1536, 8)	DeConv2D block (d_9)	(4096, 3072, 1)
512	Conv2D block (c_2)	(1024, 768, 16)	DeConv2D block (d_8)	(2048, 1536, 8)
256	Conv2D block (c_3)	(512, 384, 32)	DeConv2D block (d_7)	(1024, 768, 16)
128	Conv2D block (c_4)	(256, 192, 64)	DeConv2D block (d_6)	(512, 384, 32)
64	Conv2D block (c_5)	(128, 96, 128)	DeConv2D block (d_5)	(256, 192, 64)
32	Conv2D block (c_6)	(64, 48, 256)	DeConv2D block (d_4)	(128, 96, 128)
16	Conv2D block (c_7)	(32, 24, 512)	DeConv2D block (d_3)	(64, 48, 256)
8	Conv2D block (c_8)	(16, 12, 1024)	DeConv2D block (d_2)	(32, 24, 512)
4	Conv2D block (c_9)	(8, 6, 2048)	DeConv2D block (d_1)	(16, 12, 1024)

connected to multiple layers. The information propagates forward layer-to-layer from input images to output images with connected neurons. In this particular problem inputs are needlet coefficients of frequency maps $\beta_{j,\nu}(\hat{n})$ and output is needlet coefficients of CMB map. We choose 143 GHz to be the channel frequency of the output of the network. We adopt the U-net architecture [52] and apply it to spherical data at needlet space. We refer to this ML model **Deep Needlet**. The details of input and output data structure to work on HEALPix maps in order to preserve the rotational invariance are discussed in Section 5.

Here we describe the details of the building blocks of the architecture. The U-net architecture is built upon hidden Conv2D blocks and DeConv2D blocks at different resolutions in the encoder and decoder part respectively of the network with some skip connections between two parts. The summary of the network model is shown in Table 2. The Conv2D block consists of convolution \rightarrow Batch normalisation \rightarrow Activation \rightarrow Dropout \rightarrow convolution \rightarrow Batch normalisation \rightarrow Activation \rightarrow Max – pooling. The DeConv2D block consists of upsampling \rightarrow concatenation \rightarrow convolution \rightarrow Batch normalisation \rightarrow Activation \rightarrow Dropout \rightarrow convolution \rightarrow Batch normalisation \rightarrow Activation. At each Conv2D/DeConv2D block PReLU activation [54] is applied. Each Conv2D block downgrades the map size by half through Max – pooling operation. Similarly, each DeConv2D block doubles the size of the input maps of the previous layer. To pass the information from the contracting path to the expansion path, a *skip connection* is used between hidden layers of encoder and decoder blocks at each resolution. For example, c_9 is concatenated to corresponding same resolution maps at layer d_1 . The same is applied between c_n th layer and d_{10-n} th layer. We choose the kernel size of 4×4 for each convolution and set *stride* to 2. To prevent over-fitting, we use Dropout that randomly zeroes some of the units with a probability of 10%. We add Batch normalization in each hidden layer to ensure inputs of the next layer remain normalised for smooth training. Padding is applied to keep the same image size after application of convolution. The number of the filters applied to each convolution is displayed in the third quantity of the corresponding output layer shape listed in Table 2. We use least absolute deviation as the loss function to minimise the error between predicted values and true output values,

$$\mathcal{L} = \text{mean}(|Y - f_{w,b}(\mathbf{X})|), \quad (3.1)$$

and Adam [55] optimizer is used in training to minimize the loss function.

Since the needlet coefficient maps are at different resolutions for different bands, we apply a different version of the network to different bands keeping the fundamental layers of the network same for all bands. For example, in Table 2 we describe the network design for maps at $\text{Nside}=1024$. Since at bands 9–11 input/output maps are at $\text{Nside}=1024$, the network architecture used for this band is as described in Table 2. Similarly, since from band 6 to band 8 the input and output

maps have a resolution of $N_{\text{side}}=512$, the network architecture used for these bands starts at c_2 layer and ends at d_8 layer with the final output shape of (2048, 1536, 1) that corresponds to N_{side} of output map of 512. The same is followed for other bands according to the N_{side} resolution of the input/output maps at respective bands.

4 Data

4.1 simulations

The simulated data sets used in network training and testing include the instrument specifications of *Planck* CMB experiment. The maps used in this work include the CMB and foreground contribution from thermal dust, synchrotron, free-free, AME, line emission of CO, thermal and kinetic Sunyaev-Zeldovich (tsz and ksz), and CIB. We do not include any point sources since [50] has reported inclusion of point sources causes network training insufficient. The treatment of point sources in the analysis of CMB recovered from real data is discussed in Section 7. The CMB maps are Gaussian random realisations of given lensed CMB C_ℓ s computed using CAMB¹. To capture the full spread of Λ CDM parameter space, in CAMB, we use a different set of six Λ CDM parameters drawn from Gaussian distribution with given best-fit and 1σ standard deviation values of *Planck* 2018 result [56].

For the Galactic foregrounds, we use two set of models of thermal dust, synchrotron, free-free, and AME available in PYSM [57]. The sets consist of following configurations:

Configuration – 1: d1s1f1a2: The d1 thermal dust model follows single modified blackbody (MBB) spectrum that uses 545 GHz dust maps for intensity, and temperature and spectral index maps from Commander analysis of *Planck* 2015 data [58]. The synchrotron model s1 uses power law scaling. The model uses Haslam 408 MHz maps as synchrotron template [59] and spatially varying synchrotron spectral index map derived by fitting 408 MHz and WMAP 23 GHz polarization data using model 4 of [60]. The free-free model f1 uses free-free emission template of Commander at 30 GHz and scale it to other frequencies using power law index of -2.14 . The AME model a2 uses two spinning dust components of Commander [58] and frequency scaling is done using SpDust2 code [61].

Configuration – 2: d7s1f1a2: We replace the dust model of previous configuration with d7 that uses dust model as described in [62] based on different dust grains composition. This configuration is only used in Section 6.1 as a test samples to assess the ability of trained network to subtract the unseen dust complexity. No network training is performed using this configuration.

The foreground emissions are too complex in real-world scenarios, especially with complicated special variations of spectral parameters and amplitudes. We want to train the network with the ability of predicting the unseen data which requires a sufficient generalization of foreground training samples. In order to increase the independent training samples, we randomize the spectral parameters in each realization which matches within the prior knowledge of observational errors [63–65]. This helps the training process to reduce the dependency on a particular foreground template. However, we add a single realization of CO, tsz, ksz and CIB to the above configurations. These maps are simulated using PYSM3 and due to the lack of the scope to randomise these templates within the current simulation framework, we use only one realisation of these components. The impact of this is in detail studied in Section 6. We use co1 model for CO line intensities at central frequencies 115.3, 230.5 and 345.8 GHz. The CO emission maps obtained from *Planck* data using MILC [66] method are used as templates. The CIB and SZ maps are simulated using *WebSky* cib1, tsz1 and ksz1 models [67]. We use band pass integration at each frequency band using *Planck* bandpass profiles at *Planck* frequencies.

We use 300 FFP10 noise realizations of *Planck* [58]. All these maps are downgraded to $N_{\text{side}}=512$ on HEALPix grid [68] and smoothed to the common beam FWHM discussed in previous section.

¹<https://camb.info>

4.2 Planck data

We use *Planck* PR3 temperature data [8] to apply to the trained ML model. We use all LFI maps and HFI maps at 100–353 GHz. All the maps are smoothed to a common beam FWHM=7.27' and downgraded to $N_{\text{side}} = 512$ before application to the ML model. A special care in beam deconvolution to LFI maps is adopted due to their larger beam size than common beam FWHM which we discuss in Section 6.2. We also use CMB temperature maps produced by Spectral Matching Independent Component Analysis (SMICA) and NILC provided in PR3 data release [69] for comparison with the CMB map produced in this work. In power spectrum estimation from simulated maps, the Galactic mask (GAL70 hereafter) provided in *Planck* 2018 data release is used that comprises 70% sky. For real data analysis in Section 7, we use the common intensity mask of *Planck* 2018 result. This mask is produced from CMB solutions of four pipelines (NILC, SMICA, COMMANDER and SEVEM) setting the thresholds of $3 \mu K$ to standard deviation maps at large angular scales (FWHM = $80'$) and $10 \mu K$ at small scales (FWHM = $10'$). We multiply point source masks of *Planck* [70] to common intensity mask to produce a final confidence mask. This final mask excludes the Galactic plane and compact objects and retains approximately 76 % of the sky. We refer to this mask PL76 hereafter.

5 data processing

We simulate a set of 1200 mock data in Section 4.1. We use 1000 of these realisations for training, 100 realisations for validation and 100 realisations as test sets. Our network is designed to perform on 2D array. Therefore we approximate the HEALPix arrays of needlet coefficients to rectangular grids following the scheme of [51] before implementing the maps to the network. The HEALPix maps in NESTED ordering are arranged in 12 square grids of size $N_{\text{side}} \times N_{\text{side}}$ and then maps are placed in rectangular grids of size $4N_{\text{side}} \times 3N_{\text{side}}$. [51] has reported this rearrangement of HEALPix data can approximate the convolution over the sphere to a good extent. The two-dimensional foreground cleaned CMB needlet coefficient maps recovered in the network output layer are projected back to the corresponding N_{side} maps. A set of normalization factors corresponding to different bands are applied to normalise the output CMB needlet coefficient maps to facilitate smoother training. The inverse transformation using the same factors is applied to network outputs to recover the CMB needlet coefficient maps during testing. The output needlet coefficient maps are finally combined to recover the CMB map at $N_{\text{side}} = 512$ following Equation 2.9.

6 Model training and CMB recovery

Our network inputs are needlet coefficients of beam-convolved frequency maps comprising CMB, foregrounds, and instrument noise. The expected outputs of the network are beam-convolved needlet coefficients of CMB temperature map. We randomly select 1000 training samples in batches of 12 for network training. We randomly add FFP10 noise realizations to each of the sky realizations. We experiment on two different frequency combinations in training. We use four HFI frequency bands, 100, 143, 217 and 353 GHz as our first choice (we call this **Experiment – 1**). In order to explore the dependencies on both low and high frequency channels, we also explore one more option of using *Planck* channels from 30 GHz to 353 GHz (we call this **Experiment – 2**) in Section 6.2. The networks are trained for 1000 epochs². The training procedure is performed in NVIDIA Dell R720 GPU and is completed in four days. We set learning rate to 0.1 at starting and gradually decreases to 10^{-6} at later epochs. After completion, we find the training loss function reaches approximately below 0.5 for all the needlet bands. Validation loss also to be found to reach to same level.

Once we validate the network with a validation set of 100 realizations, we apply the trained networks to test samples. First, we examine the network trained with foreground configuration comprising Galactic components only at 100–353 GHz. In this section, we compare all the results recovered from the network model with corresponding results obtained from the NILC pipeline. In the left panel

²Each epoch refers to a single pass of the training dataset in batches of 12 through the network during the training procedure.

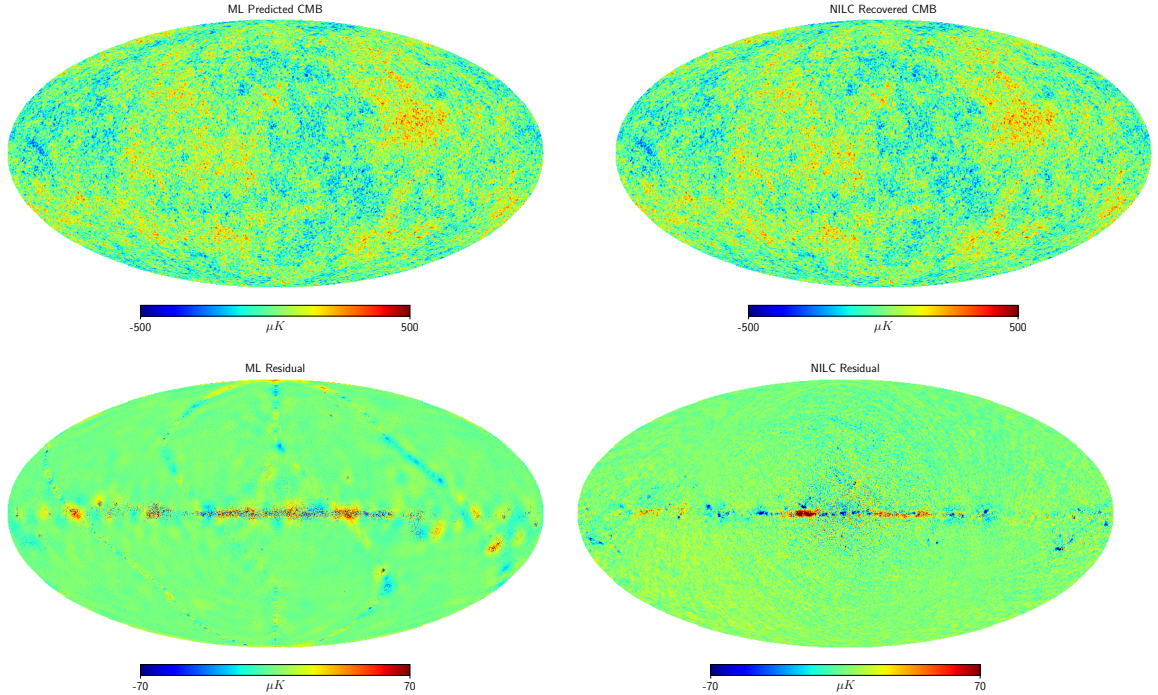


Figure 2: The ML recovered CMB (upper left), NILC recovered CMB (upper right), residual leakage in recovered CMB for ML (lower left) and NILC (lower right).

of Figure 2, we present the resulted foreground cleaned CMB map (upper left) and corresponding residual map (lower left) for one test simulation. For comparison, in the right panel of Figure 2, we present the NILC recovered CMB map (upper right) and corresponding residual (lower right) for the same realization. With a visual inspection, one can see the residual leakage in ML recovered CMB map is mostly present at the Galactic plane and residual is less compared to residual leakage using NILC. The power spectra of residual maps are more deeply assessed in later of this section. The mean absolute error (MAE) w.r.t the reference CMB maps, $\langle |Y^{Reference} - Y^{Predicted}| \rangle$ is found to be $4.25 \mu K$ for ML recovered CMB maps over GAL70. The same is found to be $10.26 \mu K$ for NILC-recovered CMB maps. We examine the 1D statistics, the probability density functions (PDFs) of difference of needlet coefficients of ML output and reference CMB map at all needlet bands in Figure 3. At band 1, we find the largest mismatch between the needlet coefficients of reference map and recovered map because of the large-scale leakage of foregrounds to recovered CMB. This is due to the approximation of HEALPix maps to rectangular grids that affect the large-scale patterns of foregrounds during convolution in hidden layers. For the rest of the bands, the dispersion of difference increases from larger (band 1) to smaller (band 11) angular scales.

We evaluate the mean angular power spectrum (brown) from recovered CMB maps and compare with theoretical power spectrum (black) and mean power spectrum of true reference CMB maps (green) in upper left panel of Figure 4. The power spectra are estimated using Xpo1 [71] over 2 degree apodized mask GAL70. In the lower panel, we display the mean deviation and 1σ errorbar of recovered power spectra w.r.t. power spectra of reference maps binned with $\Delta\ell = 30$. For comparison with NILC, we over plot the same results (dark gray) for recovered CMB maps using NILC. A small multiplicative bias ($< 0.7\%$) was found in mean power spectrum of recovered CMB maps from network model over entire angular scales. This is mainly due to the use of the map-based loss function in network modeling. In order to investigate the bias in more details, we cross-correlate the residual of recovered map with input reference map. In lower left panel of Figure 4, we present the power spectra of the cross-correlation power spectra for both methods. One can find NILC residual does not

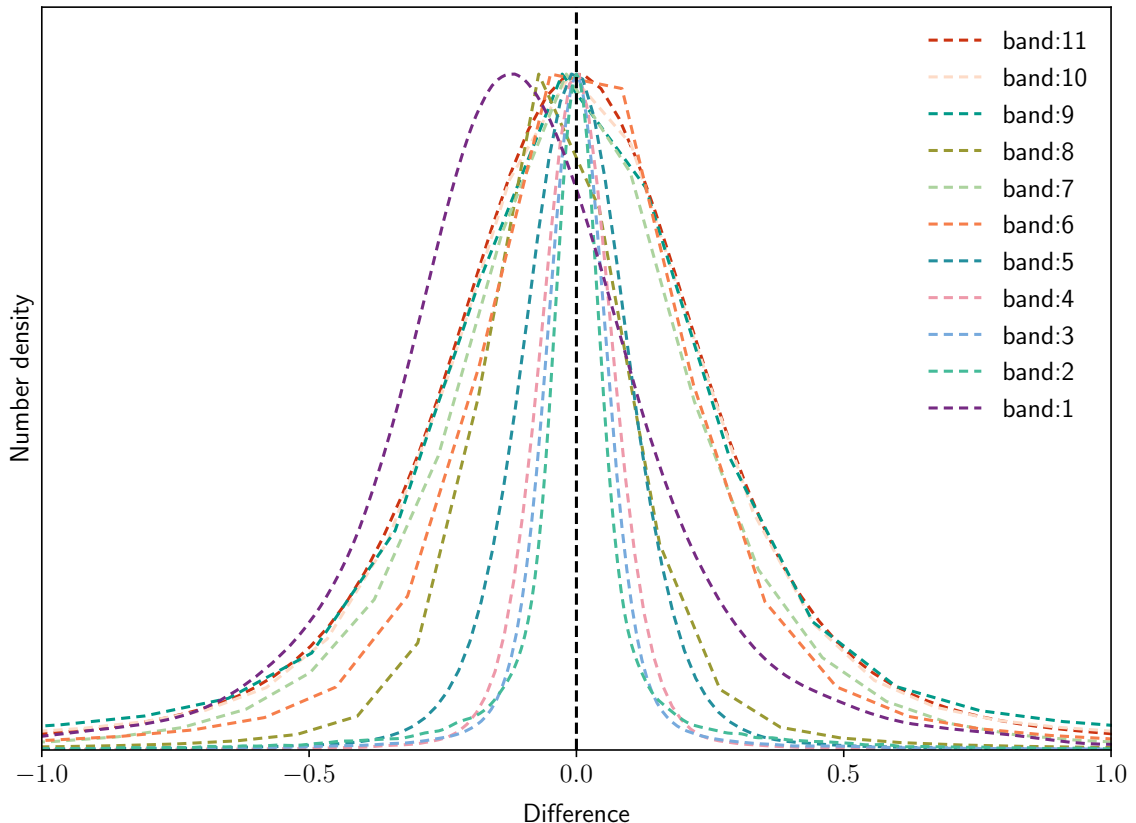


Figure 3: The PDF of the difference between the needlelet coefficient maps from network output and reference CMB at needlelet bands for one test sample. The differences at band 1 to 5 are divided by 10 to keep x-axis range fixed for all bands for easy comparison.

have any correlation with reference CMB map exhibiting no leakage of CMB signal to residual map. On contrary, same correlation for ML model shows consistent negative values at all scales exhibiting biased recovery of CMB map from network model. We correct this bias using a quadratic fit to the residual power spectra following [50] and find the bias is significantly reduced at scales $\ell \lesssim 1100$. A similar assessment in map level may alter the information of recovered CMB map and therefore we do not attempt to correct the bias in map level. This same bias correction is followed to the Section 6.2 and Section 7 using same factors estimated in this section. The power spectrum from ML predicted CMB maps agrees with the theoretical power spectrum at $\ell \lesssim 1100$. Below this scale the recovered CMB is substantially underestimated by network and therefore ΔD_ℓ is systematically negative as shown in lower panel.

Next we evaluate the network trained including the extragalactic components. A 10% increase of MAE in recovered map is found as compared to the results of former configuration. For CMB recovered from NILC, the same increment of MAE is only 5%. We also find a larger bias ($< 1.3\%$) in power spectrum of recovered CMB map as compared to previous configuration. This is plausibly due to limitation of use of multiple realizations of extragalactic components in network training. In upper right panel of Figure 4, we present the corresponding results of mean estimated power spectra from recovered maps, true reference maps, NILC recovered CMB maps and deviation from power spectra of reference maps after bias correction. The disagreement between power spectrum from NILC results and ML results start at larger ℓ (~ 600) compared to previous configuration. This is partly due our limitation to use of multiple realisations of extragalactic components during training as stated above.

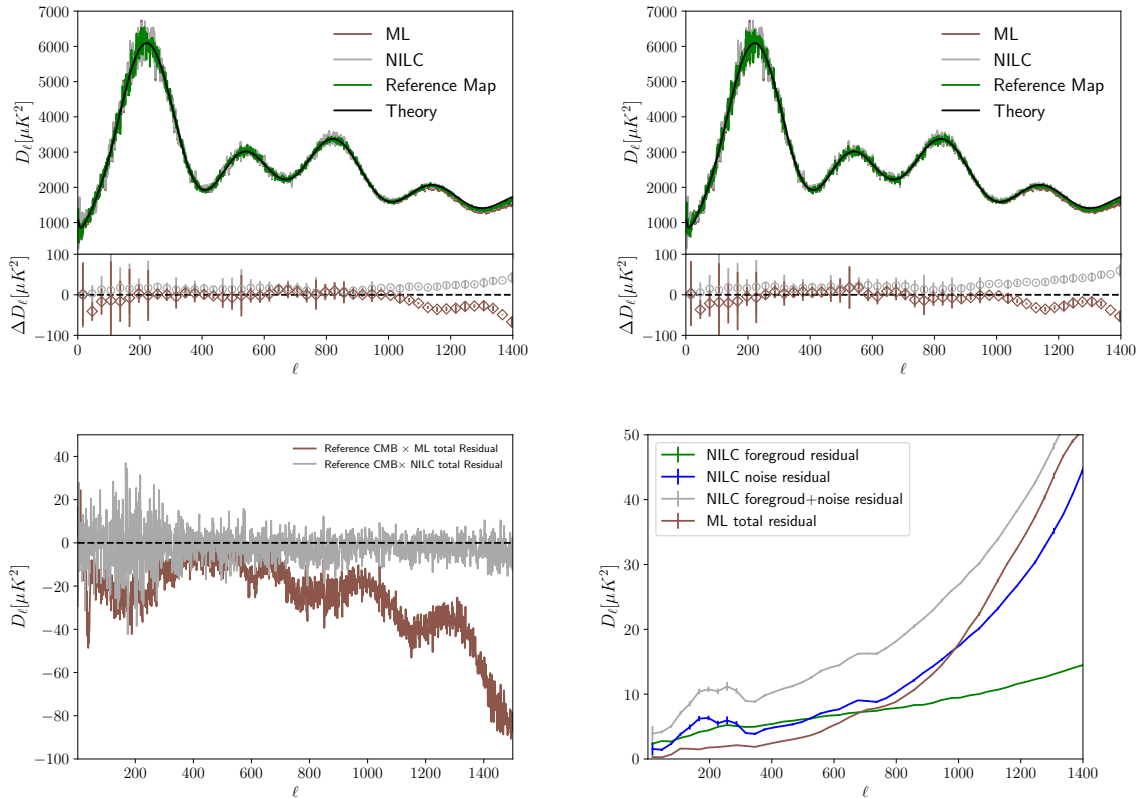


Figure 4: Upper left panel: Mean TT power spectra from 100 realizations of ML (brown) and NILC (dark gray) recovered CMB maps and true reference CMB maps (green) estimated over GAL70 mask for foreground configuration comprising only Galactic components. In bottom panel, we show the mean and 1σ errorbars of deviation of recovered power spectra w.r.t power spectra of reference CMB maps binned with $\Delta\ell = 30$. Theoretical TT power spectra is shown in solid black line. Upper right panel: Same as upper left panel for foreground configuration comprising both Galactic and extragalactic components. Lower left panel: Bias in recovered CMB maps using both methods. The cross-correlation between residual map of NILC and reference CMB map (dark gray) is consistent with zero. A similar cross-correlation for residual map for network model (brown) is consistently negative exhibiting leakage of the CMB signal to residual at all scales. Lower right panel: Mean residual power spectra of noise (blue), foregrounds (green) and total (noise + foregrounds, in dark gray) present in NILC recovered CMB maps. The mean of total residual power spectrum in ML recovered CMB maps is shown in brown corrected for bias.

We assess the power spectra of residual leakage to the recovered CMB map. The results are displayed in lower right panel of Figure 4. We show the mean power spectra of residuals from foregrounds (green), noise (blue) and foregrounds + noise (dark brown) for NILC and total residual (brown) for ML recovered CMB maps. The residual power spectrum for ML method is corrected for bias. The residual power spectrum for recovered CMB using the network model is less than the same for NILC total residual throughout the scales. After $\ell \sim 1100$ this is majorly due to less effectiveness of bias correction after $\ell \sim 1100$ for ML recovery discussed above. Below $\ell \sim 700$, the residual power spectrum for the network model is even less than same of foreground residual for NILC. This exhibits better performance of foreground subtraction of network model that is based on the morphological features of non-Gaussian Galactic foregrounds that are dominantly present at large scales. On the contrary, NILC method is blind to any spatial features of the foreground components. However, CMB recovery of the network model is always prone to spatial complexities of foregrounds. This has been discussed in the next section.

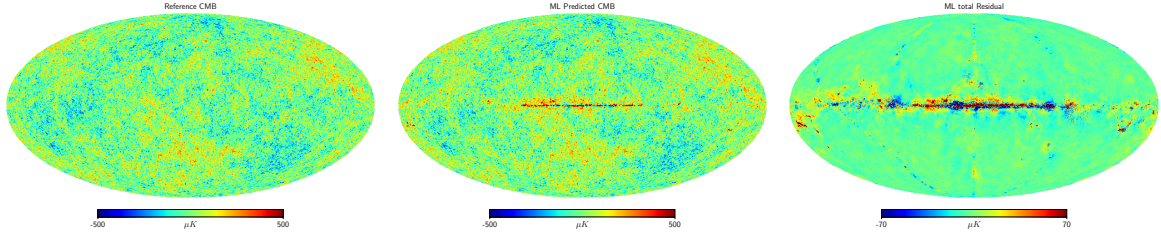


Figure 5: Left panel: Reference CMB map. Middle panel: ML recovered CMB map using `Configuration – 2` as a test simulation. Right panel: Total residual in ML recovered CMB map.

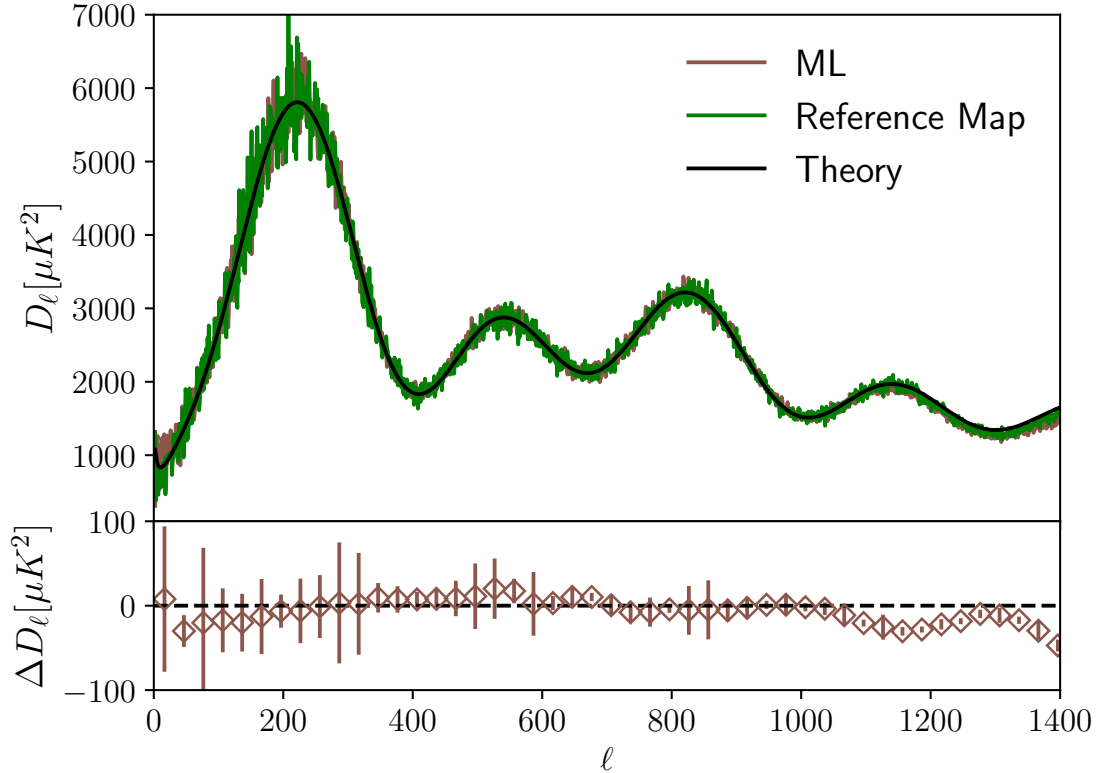


Figure 6: The mean power spectrum of recovered CMB maps using `Configuration – 2` as test simulations estimated over `GAL70` mask. The green curve is the mean power spectrum of reference CMB maps. Lower panel shows the deviation of recovered power spectrum from true power spectrum of reference maps.

6.1 Testing the impact of dust complexity

The network described above is trained with `Configuration – 1` that includes `PYSM d1` dust model. The dust has a significant foreground contribution between 100–353 GHz. Therefore, to test the robustness of the model, we evaluate the trained network model with `Configuration – 2` replacing the dust model with `PYSM d7` model. In Figure 5, we present the input reference map (left panel), the recovered CMB map (middle panel) and the residual (right panel) for one test sample. The recovered CMB map contains a larger residual compared to the previous result (see Figure 2), especially in the Galactic plane ($|b| < 15$ degree). The MAE is found to be $\sim 14 \mu K$ to which the maximum contribution is seen from the first two needlet bands where the large-scale Galactic signals have a

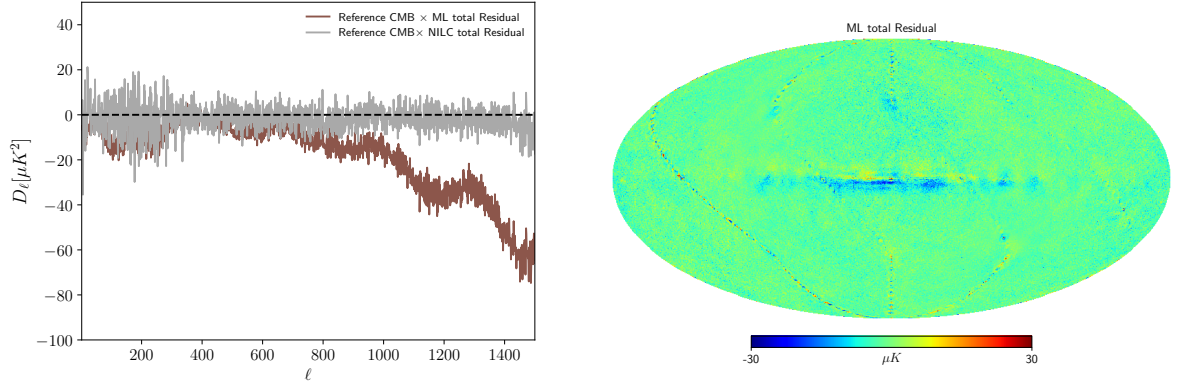


Figure 7: Left panel: Bias in recovered CMB maps for **experiment - 2** using both cleaning method. The bias in ML recovered CMB map is considerably reduced for **experiment - 2** at $\ell < 1000$ as compared to **experiment - 1**. Right panel: The corresponding residual in recovered CMB map.

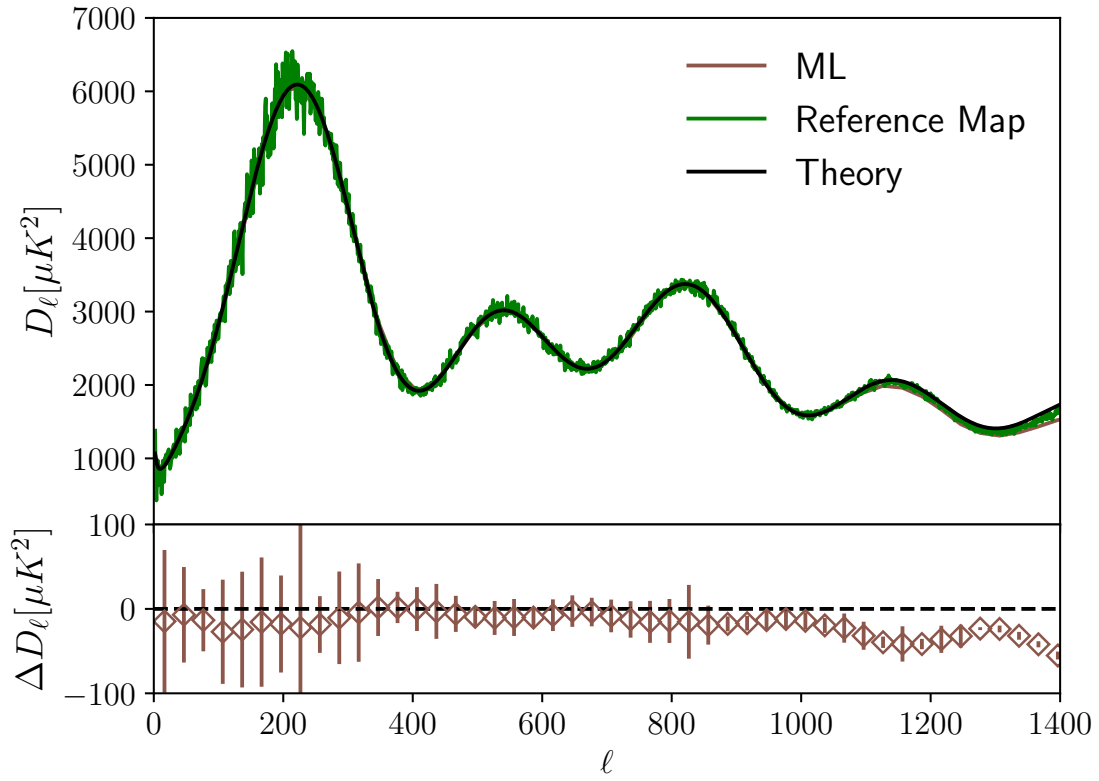


Figure 8: Same as Figure 6 for predicted CMB using trained network for **experiment - 2**.

maximum contribution. However, the resulted power spectrum of recovered CMB shown in Figure 6 does not noticeably change with the updated dust model. The estimated power spectrum is corrected for bias following the same factors in the previous section. This suggests over 70% intermediate and high latitude sky the performance of the trained network remains same for the updated dust model.

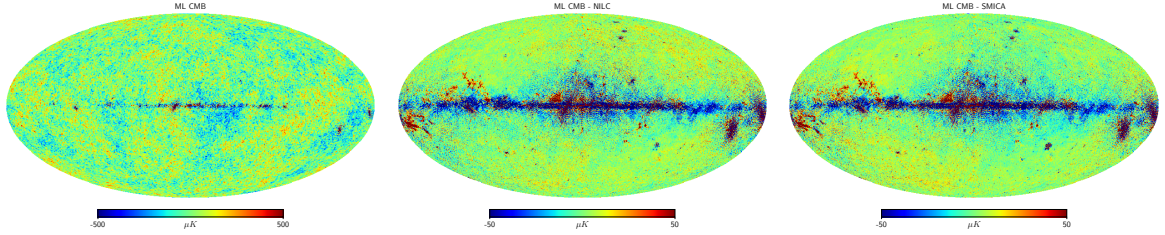


Figure 9: Left panel: ML recovered CMB from *Planck* data evaluated using network trained within 30-353 GHz in Section 6.2. This map is at $\text{FWHM} = 7.27'$. Middle panel: Difference between recovered our CMB and NILC CMB of *Planck* legacy data. Right panel: Difference between recovered our CMB and SMICA CMB of *Planck* legacy data. The both residual maps are at $10'$ resolution.

6.2 Dependency on choice of frequency channels

In this section, we test whether additional information using more frequency channels improves the CMB recovery using the network model. Since *Planck* LFI 30, 44 GHz and 70 GHz channels provide additional information of foregrounds and CMB at angular scales $\ell \lesssim 650$ and $\ell \lesssim 1000$ respectively, we experiment (**experiment – 2**) the performance of **Deep Needlet** adding these three additional channels in training the model. We do not consider the last two HFI channels since noise power spectra are much larger than the CMB signal at 545 and 857 GHz. For network training of **experiment – 2**, we follow a similar procedure discussed in Section 6. Since LFI channels have resolutions lower than common beam FWHM, the convolution of LFI maps with $\text{FWHM} = 7.27'$ does not add any additional information and boosts the noise levels. Therefore we give special attention to using these channels in needlet bands. Following [69] (see Appendix B of this paper), in beam deconvolution, we only consider those multipoles for which the ratio between beam transfer function of respective LFI channels and common beam FWHM of $7.27'$ is below 0.01. Therefore the LFI channels are used for those needlet bands where harmonic contents of the deconvoluted LFI maps span the the entire bandwidth of the given needlet band. This procedure restricts the use of 30 and 44 GHz channels up to band 7. For a similar reason, 70 GHz channel is used up to band 8. After validating the network with 100 validation sets, we evaluate the network using 100 test simulations. In Figure 7 we show the bias in recovered CMB (left panel) and corresponding residual map (right panel) for one set of test simulations. Residual leakage is seen significantly reduced especially at large angular scales compared to **experiment – 1** (see Figure 2). The MAE is found to be $2.43 \mu K$ corresponds to $\sim 40\%$ reduction compared to results in Section 6. Also since 30 and 44 GHz add CMB information at $\ell < 650$ and 70 GHz adds additional CMB information at $\ell < 1000$, the bias in recovered CMB maps significantly reduced at $\ell \lesssim 1000$. We show the mean power spectrum from recovered maps and deviation w.r.t power spectra of reference CMB maps binned with $\Delta\ell = 30$ in Figure 8. We see the recovered power spectrum is more consistent with the power spectrum of the reference map. However, we do not see much improvement in small-scale bias correction at $\ell > 1100$. This illustrates incorporation of more information with additional channels improves the network performance and noise levels do not have much relevance in bias production. We discuss the role of instrument noise levels in network performance in Appendix A in more detail.

7 Application to *Planck* data

With the neural network model trained in Section 6.2, we recover the CMB temperature map from *Planck* PR3 data. All LFI channels and HFI 100–353 GHz maps contribute to this reconstruction. The maps are deconvolved with respective beam FWHM and convolved with common beam $\text{FWHM} = 7.27'$. We take precautions in LFI beam deconvolution as discussed in Section 6.2. The resulting CMB map at $7.27'$ resolution is displayed in the left panel of Figure 9. To compare with *Planck* legacy products of CMB temperature, we show the difference between our recovered CMB map and NILC and SMICA CMB maps of *Planck* 2018 results [69] in the middle and right panels respectively. These

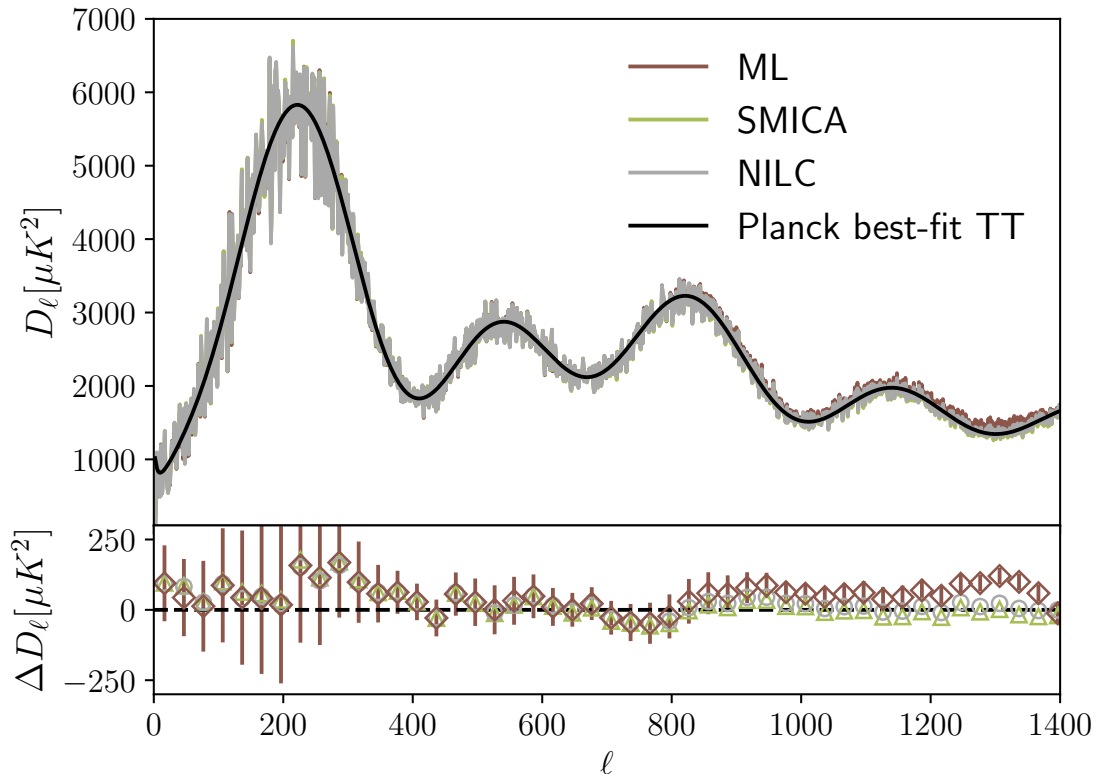


Figure 10: The power spectrum from ML recovered CMB using *Planck* data between 30-353 GHz estimated over PL76 mask. In the lower panel, we present the deviation from *Planck* best-fit theoretical power spectrum within bin of $\Delta\ell = 30$. The errorbars are cosmic variance at corresponding bin.

difference maps are shown at $10'$ resolution. Above the Galactic plane ($|b| > 15$ degree) the difference is present in small scales. The MAEs of recovered CMB – NILC CMB and recovered CMB – SMICA CMB are found to be $9.07 \mu K$ and $8.67 \mu K$ respectively after masking the Galactic pixels which is close to the MAE of SMICA CMB – NILC CMB that is $4.02 \mu K$.

We estimate the power spectrum of the reconstructed CMB map and compare it with SMICA and NILC CMB power spectra in Figure 10. All power spectra are estimated over PL76 mask and corrected for respective beams. It is important to note that we do not consider the simulation of bright sources in training samples. Therefore recovery of the map at the pixels of compact objects is inaccurate. Therefore, we use PL76 mask in analysis of recovered map that excludes pixels of the bright sources. The bias correction is implemented to estimated power spectrum of ML recovered CMB following Section 6.2 for the sake of robustness. The best fit *Planck* power spectrum [56] is shown in black solid line. In the lower panel, we show the deviations of power spectra from *Planck* best fit value binned with $\Delta\ell = 30$. The 1σ errorbars shown here is the cosmic variance limit. All power spectra match up to $\ell \simeq 900$. The discrepancies between real data and simulated data used in training resulted in an increase presence of foreground residuals in the recovered CMB map. There is a small disagreement between the power spectrum of our recovered CMB and SMICA and NILC CMB map at $\ell \gtrsim 900$. To find the source of disagreement, we repeat the same analysis on *Planck* FFP10 simulations [72]. There we find a small disagreement between the estimated power spectrum from the recovered map and *Planck* legacy data is present in large scales ($\ell < 300$) instead of small scales. This illustrates the source of disagreement for PR3 data might be caused by instrument systematics present

in PR3 data and therefore consistency check is beyond the scope of this paper since systematics are not taken into account in model training.

8 Discussion and Summary

This work presents a new development of a ML model on needlet space, namely **Deep Needlet** to recover the CMB temperature map from multi-frequency data at mm and submm bands. The model is trained with simulated full sky data that exhibits a diverse range of foreground spectral features and CMB temperature for a spectrum of cosmological parameters distributed within 1σ standard deviation of *Planck* 2018 best-fit results. We first test the trained network on simulations incorporating a similar complexity aligned to the complexity of training samples and compare the results with NILC-recovered CMB for the same realizations. We find MAE for ML predicted CMB is less than same for NILC recovered CMB map. A clearer idea about the efficiency of the methods is established in comparison of residual power spectra from both methods. We show residual power spectrum for ML predicted CMB is less than the same from NILC throughout the angular scales. The power spectrum of recovered CMB closely matches the true power spectrum of the reference CMB map at $\ell < 1100$. Subsequently, we examine the performance of CMB recovery using the network model for foreground complexity not aligned to the complexity of training samples. For this case, our network returns larger residuals in recovered CMB at the Galactic plane and at intermediate to high Galactic regions over 70% sky, it recovers the CMB with high accuracy. This is evident in the recovered power spectrum estimated over GAL70 which matches accurately with the true power spectrum of reference CMB map at $\ell < 1100$.

We discuss the improvement of CMB recovery with the introduction of additional large-scale information adding *Planck* LFI channels in network training. This analysis shows a better match between the power spectrum of recovered CMB map and reference CMB power spectrum.

Our findings demonstrate the intrinsic challenges of feature extraction of the ML model. Due to the use of pixel-based loss function, the network model recovers biased CMB maps at all scales. The bias increases towards the smaller angular scales. We examine the nature of bias in estimated CMB for a model trained without instrument noise and with larger frequency coverage. We find the bias is intrinsic to the model due to the use of a pixel-based loss function in the ML model. A potential solution to this issue could be the use of a hybrid loss function that includes two-point correlation along with pixel-based loss function [73].

After being shown to work on simulations, we apply the network to *Planck* PR3 data. We find recovered CMB map is very similar to the CMB temperature maps from SMICA and NILC pipelines. The power spectrum of all CMB maps match quite accurately at $\ell < 900$. After that scale, there is a small disagreement between the power spectra of recovered maps and NILC and SMICA CMB maps. This is due to a limitation of the use of instrument systematics in training sets that limits network performance in CMB recovery in presence of instrument systematics in the real data. In this work, we only consider temperature maps to demonstrate the network performance. In future work, one avenue is to extend the presented technique to polarization data.

9 Acknowledgment

All the computations in this paper are done using the HPC Nandadevi and Kamet (<https://hpc.imsc.res.in>) at the Institute of Mathematical Sciences (IMSc), Chennai, India. Da acknowledge financial support by the Department of Atomic Energy, India that funded the postdoctoral position to department of theoretical physics at The Institute of Mathematical Sciences (IMSc). A partial financial support was provided by the Spanish Ministry of Science and Innovation under the project PID2020-120514GB-I00, and the Severo Ochoa Programs SEV-2015-0548 and CEX2019-000920-S for postdoc position at Instituto de Astrofísica de Canarias (IAC). DA acknowledges support from the ACIISI, Consejería de Economía, Conocimiento y Empleo del Gobierno de Canarias and the European Regional Development Fund (ERDF) under grant with reference ProID2020010108, and Red de Investigacion RED2022-134715-T funded by MCIN/AEI/10.13039/501100011033. This project uses the publicly available codes; *cmbnncs* (<https://github.com/Guo-Jian-Wang/cmbNNCS>), PyTorch,

PYSM, HEALPix, CAMB, and Xpol. DA would like to thank Guo-Jian Wang and Benjamin Wandelt for useful discussion of ML techniques. DA would like to thank Jacques Delabrouille for his useful suggestions on NILC pipeline.

Appendices

A Dependency on instrument noise

In this section, we test the impact of instrument noise on performance of the ML model. [51] has discussed in details the performance of U-net architecture with 50% and 70% reduced instrument noise levels of *Planck* HFI channels (100–353 GHz). They find the network performs with similar accuracy when they train the network using four HFI (100–353 GHz) channels with *Planck* noise and using two HFI channels (143 and 217 GHz) with 70 % reduced *Planck* noise. On the contrary, we find the residual can only be reduced with the incorporation of more channels without reducing the *Planck* noise levels. It is important to note that the total residual in ML recovered CMB is a collective contribution of biased prediction of CMB of ML model and foreground and noise present in the frequency maps as discussed in the main text. In this section, we discuss whether the source of bias is *Planck* instrument noise or an intrinsic feature of U-net architecture at small scales. Therefore we train the ML model without instrument noise and repeat our analysis of section 6.

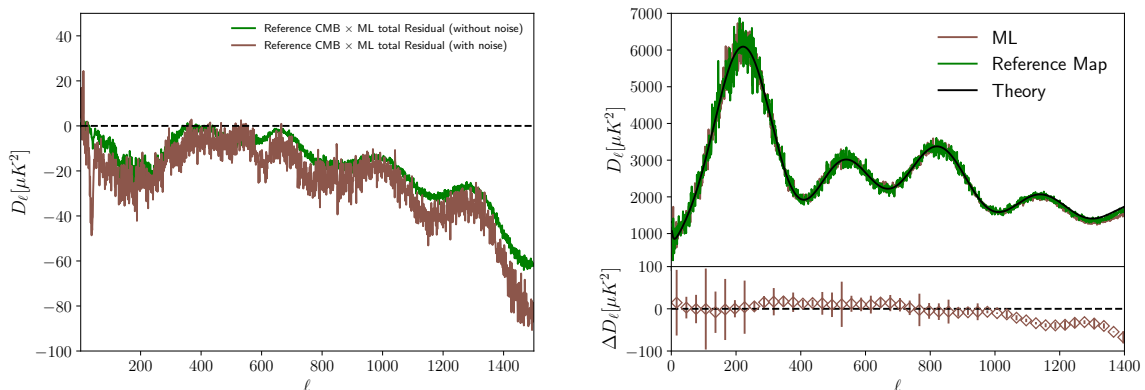


Figure 11: Left panel: Comparison of bias in ML recovered CMB from trained network with (*dark gray*) and without (*green*) instrument noise. Right panel: Corresponding CMB power spectra and residual estimated over GAL70 and corrected for bias.

In the left panel of Figure 11 we compare the bias in recovered CMB from the model trained with (*dark gray*) and without (*green*) instrument noise. We do not find any significant difference in cross-correlation between input reference CMB and residual maps for two cases. In the right panel of Figure 11 we display the estimated power spectrum corrected for bias following the procedure in Section 6. Comparing this result with the upper right panel of Figure 4, we see the estimated power spectrum matches with similar accuracy at $l < 1100$ for both cases and approximately a similar bias is present in residual maps at small scales. However, we see a small improvement in residual bias at $l < 200$. This illustrates feature extraction at small scales using U-net architecture is intrinsic to the network model and relatively independent of *Planck* instrument noise levels. This also hints biased estimation of CMB map from the network model is a major contributor to residual leakage relative to *Planck* instrument noise. It is important to note that there is a subtle difference between our ML model and the model used in [51]. We use band-filtered signals in the training process whereas [51] used full harmonic information in training. Since feature extraction depends on the type of training data sets used, two networks may cause different biases in recovered CMB maps.

References

- [1] T. P. C. P. A. R. Ade, Y. Akiba, A. E. Anthony, K. Arnold, M. Atlas, D. Barron et al., *A MEASUREMENT OF THE COSMIC MICROWAVE BACKGROUND B-MODE POLARIZATION POWER SPECTRUM AT SUB-DEGREE SCALES WITH POLARBEAR*, *The Astrophysical Journal* **794** (2014) 171.
- [2] R. Génova-Santos, J. A. Rubiño-Martín, R. Rebolo, A. Peláez-Santos, C. H. López-Caraballo, S. Harper et al., *QUIJOTE scientific results - I. Measurements of the intensity and polarisation of the anomalous microwave emission in the Perseus molecular complex*, *MNRAS* **452** (2015) 4169 [[1501.04491](#)].
- [3] N. Galitzki, *The Simons Observatory: Project Overview*, 10, 2018, [1810.02465](#).
- [4] R. Gualtieri, J. Filippini, P. Ade, M. Amiri, S. Benton, A. Bergman et al., *Spider: Cmb polarimetry from the edge of space*, *Journal of Low Temperature Physics* **193** (2018) 1112.
- [5] J. H. Kang, P. A. R. Ade, Z. Ahmed, R. W. Aikin, K. D. Alexander, D. Barkats et al., *2017 upgrade and performance of BICEP3: a 95GHz refracting telescope for degree-scale CMB polarization*, in *Millimeter, Submillimeter, and Far-Infrared Detectors and Instrumentation for Astronomy IX*, J. Zmuidzinas and J.-R. Gao, eds., vol. 10708 of *Society of Photo-Optical Instrumentation Engineers (SPIE) Conference Series*, p. 107082N, July, 2018, [1808.00567](#), DOI.
- [6] S. K. e. a. Choi, *The Atacama Cosmology Telescope: A Measurement of the Cosmic Microwave Background Power Spectra at 98 and 150 GHz*, *arXiv e-prints* (2020) arXiv:2007.07289 [[2007.07289](#)].
- [7] SPTPOL COLLABORATION collaboration, *Measurements of b-mode polarization of the cosmic microwave background from 500 square degrees of sptpol data*, *Phys. Rev. D* **101** (2020) 122003.
- [8] Planck Collaboration I, *Planck 2018 results. I. Overview and the cosmological legacy of Planck*, *arXiv e-prints* (2018) arXiv:1807.06205 [[1807.06205](#)].
- [9] S. Hanany, M. Alvarez, E. Artis, P. Ashton, J. Aumont, R. Aurlien et al., *PICO: Probe of Inflation and Cosmic Origins*, *arXiv e-prints* (2019) arXiv:1902.10541 [[1902.10541](#)].
- [10] M. Hazumi et al., *LiteBIRD: A Satellite for the Studies of B-Mode Polarization and Inflation from Cosmic Background Radiation Detection*, *J. Low Temp. Phys.* **194** (2019) 443.
- [11] D. Adak, A. Sen, S. Basak, J. Delabrouille, T. Ghosh, A. Rotti et al., *B-mode forecast of CMB-Bhārat*, *MNRAS* **514** (2022) 3002 [[2110.12362](#)].
- [12] K. Ichiki, *CMB foreground: A concise review*, *Progress of Theoretical and Experimental Physics* **2014** (2014) 06B109.
- [13] M. Tegmark, *How to measure cmb power spectra without losing information*, *Phys. Rev. D* **55** (1997) 5895.
- [14] J. Delabrouille, J.-F. Cardoso and G. Patanchon, *Multidetector multicomponent spectral matching and applications for cosmic microwave background data analysis*, *Monthly Notices of the Royal Astronomical Society* **346** (2003) 1089 [<https://academic.oup.com/mnras/article-pdf/346/4/1089/18647087/346-4-1089.pdf>].
- [15] H. K. Eriksen, J. B. Jewell, C. Dickinson, A. J. Banday, K. M. Górski and C. R. Lawrence, *Joint Bayesian Component Separation and CMB Power Spectrum Estimation*, *ApJ* **676** (2008) 10 [[0709.1058](#)].
- [16] J. Delabrouille, J. F. Cardoso, M. Le Jeune, M. Betoule, G. Fay and F. Guilloux, *A full sky, low foreground, high resolution CMB map from WMAP*, *A&A* **493** (2009) 835 [[0807.0773](#)].
- [17] S. Basak and J. Delabrouille, *A needlet internal linear combination analysis of WMAP 7-year data: estimation of CMB temperature map and power spectrum*, *Monthly Notices of the Royal Astronomical Society* **419** (2011) 1163 [<https://academic.oup.com/mnras/article-pdf/419/2/1163/3110521/mnras0419-1163.pdf>].
- [18] R. Fernández-Cobos, P. Vielva, R. B. Barreiro and E. Martínez-González, *Multiresolution internal template cleaning: an application to the Wilkinson Microwave Anisotropy Probe 7-yr polarization data*, *Monthly Notices of the Royal Astronomical Society* **420** (2012) 2162 [<https://academic.oup.com/mnras/article-pdf/420/3/2162/3015247/mnras0420-2162.pdf>].

- [19] K. K. Rogers, H. V. Peiris, B. Leistedt, J. D. McEwen and A. Pontzen, *SILC: a new Planck internal linear combination CMB temperature map using directional wavelets*, *MNRAS* **460** (2016) 3014 [[1601.01322](#)].
- [20] M. Remazeilles, A. Rotti and J. Chluba, *Peeling off foregrounds with the constrained moment ILC method to unveil primordial CMB B-modes*, *arXiv e-prints* (2020) arXiv:2006.08628 [[2006.08628](#)].
- [21] D. Adak, *A new approach of estimating the galactic thermal dust and synchrotron polarized emission template in the microwave bands*, *Monthly Notices of the Royal Astronomical Society* **507** (2021) 4618 [<https://academic.oup.com/mnras/article-pdf/507/3/4618/40368011/stab2392.pdf>].
- [22] A. Carones and M. Remazeilles, *Optimization of foreground moment deprojection for semi-blind CMB polarization reconstruction*, *arXiv e-prints* (2024) arXiv:2402.17579 [[2402.17579](#)].
- [23] R. Stompor, S. Leach, F. Stivoli and C. Baccigalupi, *Maximum likelihood algorithm for parametric component separation in cosmic microwave background experiments*, *Monthly Notices of the Royal Astronomical Society* **392** (2008) 216 [<https://academic.oup.com/mnras/article-pdf/392/1/216/3707574/mnras0392-0216.pdf>].
- [24] S. Basak and J. Delabrouille, *A needlet ILC analysis of WMAP 9-year polarization data: CMB polarization power spectra*, *Monthly Notices of the Royal Astronomical Society* **435** (2013) 18 [<https://academic.oup.com/mnras/article-pdf/435/1/18/3843106/stt1158.pdf>].
- [25] J. Kim, P. Naselsky and P. R. Christensen, *CMB map derived from the WMAP data through harmonic internal linear combination*, *PRD* **77** (2008) 103002 [[0803.1394](#)].
- [26] J. Dick, M. Remazeilles and J. Delabrouille, *Impact of calibration errors on CMB component separation using FastICA and ILC*, *Monthly Notices of the Royal Astronomical Society* **401** (2010) 1602 [<https://academic.oup.com/mnras/article-pdf/401/3/1602/3811973/mnras0401-1602.pdf>].
- [27] S. Russell and P. Norvig, *Artificial Intelligence: A Modern Approach*. Prentice Hall, 3 ed., 2010.
- [28] H. U. Nørgaard-Nielsen, *Foreground removal from WMAP 5 yr temperature maps using an MLP neural network*, *A&A* **520** (2010) A87 [[1010.1634](#)].
- [29] S. Ravanbakhsh, J. Oliva, S. Fromenteau, L. C. Price, S. Ho, J. Schneider et al., *Estimating Cosmological Parameters from the Dark Matter Distribution*, *arXiv e-prints* (2017) arXiv:1711.02033 [[1711.02033](#)].
- [30] B. Thorne, L. Knox and K. Prabhu, *A generative model of galactic dust emission using variational autoencoders*, *MNRAS* **504** (2021) 2603 [[2101.11181](#)].
- [31] J. Chardin, G. Uhlich, D. Aubert, N. Deparis, N. Gillet, P. Ocvirk et al., *A deep learning model to emulate simulations of cosmic reionization*, *MNRAS* **490** (2019) 1055 [[1905.06958](#)].
- [32] J. Caldeira, W. L. K. Wu, B. Nord, C. Avestruz, S. Trivedi and K. T. Story, *DeepCMB: Lensing reconstruction of the cosmic microwave background with deep neural networks*, *Astronomy and Computing* **28** (2019) 100307 [[1810.01483](#)].
- [33] M. Choudhury, A. Datta and S. Majumdar, *Extracting the 21-cm power spectrum and the reionization parameters from mock data sets using artificial neural networks*, *Monthly Notices of the Royal Astronomical Society* **512** (2022) 5010 [<https://academic.oup.com/mnras/article-pdf/512/4/5010/43367464/stac736.pdf>].
- [34] S. Hassan, S. Andrianomena and C. Doughty, *Constraining the astrophysics and cosmology from 21 cm tomography using deep learning with the SKA*, *MNRAS* **494** (2020) 5761 [[1907.07787](#)].
- [35] F. Nasir, P. Gaikwad, F. B. Davies, J. S. Bolton, E. Puchwein and S. E. I. Bosman, *Deep Learning the Intergalactic Medium using Lyman-alpha Forest at $4 \leq z \leq 5$* , *arXiv e-prints* (2024) arXiv:2404.05794 [[2404.05794](#)].
- [36] E. Guzman and J. Meyers, *Reconstructing patchy reionization with deep learning*, *PRD* **104** (2021) 043529 [[2101.01214](#)].
- [37] P. Chanda and R. Saha, *An unbiased estimator of the full-sky CMB angular power spectrum at large scales using neural networks*, *MNRAS* **508** (2021) 4600 [[2102.04327](#)].

- [38] N. Jeffrey, F. Boulanger, B. D. Wandelt, B. Regalado-Saint Blancard, E. Allys and F. Levrier, *Single frequency CMB B-mode inference with realistic foregrounds from a single training image*, *MNRAS* **510** (2022) L1 [2111.01138].
- [39] F. McCarthy, J. C. Hill, W. R. Coulton and D. W. Hogg, *Signal-preserving CMB component separation with machine learning*, *arXiv e-prints* (2024) arXiv:2404.03557 [2404.03557].
- [40] P. Gawade, A. More, S. More, A. Kimura, A. Sonnenfeld, M. Oguri et al., *Neural network prediction of model parameters for strong lensing samples from Hyper Suprime-Cam Survey*, *arXiv e-prints* (2024) arXiv:2404.18897 [2404.18897].
- [41] S. Pal, S. K. Yadav, R. Saha and T. Souradeep, *Accurate and Unbiased Reconstruction of CMB B Mode using Deep Learning*, *arXiv e-prints* (2024) arXiv:2404.18100 [2404.18100].
- [42] Y.-P. Yan, G.-J. Wang, S.-Y. Li and J.-Q. Xia, *Recovering Cosmic Microwave Background Polarization Signals with Machine Learning*, *Astrophys. J.* **947** (2023) 29 [2302.13572].
- [43] R. D. Lambaga, V. Sudevan and P. Chen, *SkyReconNet: A Deep Learning Inpainting Approach for Enhanced CMB Map Reconstruction*, 2501.06139.
- [44] D. Marinucci, D. Pietrobon, A. Balbi, P. Baldi, P. Cabella, G. Kerkycharian et al., *Spherical needlets for cosmic microwave background data analysis*, *MNRAS* **383** (2008) 539 [0707.0844].
- [45] T. S. Cohen, M. Geiger, J. Koehler and M. Welling, *Spherical CNNs*, *arXiv e-prints* (2018) arXiv:1801.10130 [1801.10130].
- [46] C. "Max" Jiang, J. Huang, K. Kashinath, Prabhat, P. Marcus and M. Niessner, *Spherical CNNs on Unstructured Grids*, *arXiv e-prints* (2019) arXiv:1901.02039 [1901.02039].
- [47] N. Krachmalnicoff and M. Tomasi, *Convolutional neural networks on the HEALPix sphere: a pixel-based algorithm and its application to CMB data analysis*, *A&A* **628** (2019) A129 [1902.04083].
- [48] K. Yi, J. Chen, Y. G. Wang, B. Zhou, P. Liò, Y. Fan et al., *Approximate Equivariance SO(3) Needlet Convolution*, *arXiv e-prints* (2022) arXiv:2206.10385 [2206.10385].
- [49] N. Perraudin, M. Defferrard, T. Kacprzak and R. Sgier, *DeepSphere: Efficient spherical convolutional neural network with HEALPix sampling for cosmological applications*, *Astronomy and Computing* **27** (2019) 130 [1810.12186].
- [50] M. A. Petroff, G. E. Addison, C. L. Bennett and J. L. Weiland, *Full-sky Cosmic Microwave Background Foreground Cleaning Using Machine Learning*, *ApJ* **903** (2020) 104 [2004.11507].
- [51] G.-J. Wang, H.-L. Shi, Y.-P. Yan, J.-Q. Xia, Y.-Y. Zhao, S.-Y. Li et al., *Recovering the CMB Signal with Machine Learning*, *ApJ* **260** (2022) 13 [2204.01820].
- [52] O. Ronneberger, P. Fischer and T. Brox, *U-Net: Convolutional Networks for Biomedical Image Segmentation*, *arXiv e-prints* (2015) arXiv:1505.04597 [1505.04597].
- [53] F. McCarthy and J. C. Hill, *Component-separated, CIB-cleaned thermal Sunyaev-Zel'dovich maps from Planck PR4 data with a flexible public needlet ILC pipeline*, *Phys. Rev. D* **109** (2024) 023528 [2307.01043].
- [54] K. He, X. Zhang, S. Ren and J. Sun, *Deep Residual Learning for Image Recognition*, *arXiv e-prints* (2015) arXiv:1512.03385 [1512.03385].
- [55] D. P. Kingma and J. Ba, *Adam: A method for stochastic optimization*, *CoRR* abs/1412.6980 (2014) .
- [56] Planck Collaboration, N. Aghanim, Y. Akrami, M. Ashdown, J. Aumont, C. Baccigalupi et al., *Planck 2018 results. VI. Cosmological parameters*, *A&A* **641** (2020) A6 [1807.06209].
- [57] B. Thorne, J. Dunkley, D. Alonso and S. Næss, *The Python Sky Model: software for simulating the Galactic microwave sky*, *MNRAS* **469** (2017) 2821 [1608.02841].
- [58] Planck Collaboration, R. Adam, P. A. R. Ade, N. Aghanim, M. I. R. Alves, M. Arnaud et al., *Planck 2015 results. X. Diffuse component separation: Foreground maps*, *A&A* **594** (2016) A10 [1502.01588].
- [59] M. Remazeilles, C. Dickinson, A. J. Banday, M.-A. Bigot-Sazy and T. Ghosh, *An improved source-subtracted and destriped 408-MHz all-sky map*, *Monthly Notices of the Royal Astronomical Society* **451** (2015) 4311 [https://academic.oup.com/mnras/article-pdf/451/4/4311/3903853/stv1274.pdf].

- [60] M. A. Miville-Deschênes, N. Ysard, A. Lavabre, N. Ponthieu, J. F. Macías-Pérez, J. Aumont et al., *Separation of anomalous and synchrotron emissions using WMAP polarization data*, *A&A* **490** (2008) 1093 [0802.3345].
- [61] Y. Ali-Haïmoud, C. M. Hirata and C. Dickinson, *A refined model for spinning dust radiation*, *MNRAS* **395** (2009) 1055 [0812.2904].
- [62] B. T. Draine and B. S. Hensley, *Quantum Suppression of Alignment in Ultrasmall Grains: Microwave Emission from Spinning Dust will be Negligibly Polarized*, *ApJ* **831** (2016) 59 [1605.06671].
- [63] Planck Collaboration, A. Abergel, P. A. R. Ade, N. Aghanim, M. I. R. Alves, G. Aniano et al., *Planck 2013 results. XI. All-sky model of thermal dust emission*, *A&A* **571** (2014) A11 [1312.1300].
- [64] Planck Collaboration, P. A. R. Ade, N. Aghanim, M. I. R. Alves, M. Arnaud, M. Ashdown et al., *Planck 2015 results. XXV. Diffuse low-frequency Galactic foregrounds*, *A&A* **594** (2016) A25 [1506.06660].
- [65] J. A. Rubiño-Martín, F. Guidi, R. T. Génova-Santos, S. E. Harper, D. Herranz, R. J. Hoyland et al., *QUIJOTE scientific results - IV. A northern sky survey in intensity and polarization at 10-20 GHz with the multifrequency instrument*, *MNRAS* **519** (2023) 3383 [2301.05113].
- [66] G. Hurier, J. F. Macías-Pérez and S. Hildebrandt, *MILCA, a modified internal linear combination algorithm to extract astrophysical emissions from multifrequency sky maps*, *A&A* **558** (2013) A118 [1007.1149].
- [67] G. Stein, M. A. Alvarez, J. R. Bond, A. van Engelen and N. Battaglia, *The Websky Extragalactic CMB Simulations*, *JCAP* **10** (2020) 012 [2001.08787].
- [68] K. M. Górski, E. Hivon, A. J. Banday, B. D. Wandelt, F. K. Hansen, M. Reinecke et al., *HEALPix: A Framework for High-Resolution Discretization and Fast Analysis of Data Distributed on the Sphere*, *ApJ* **622** (2005) 759 [astro-ph/0409513].
- [69] Planck Collaboration, Y. Akrami, M. Ashdown, J. Aumont, C. Baccigalupi, M. Ballardini et al., *Planck 2018 results. IV. Diffuse component separation*, *A&A* **641** (2020) A4 [1807.06208].
- [70] Planck Collaboration, P. A. R. Ade, N. Aghanim, F. Argüeso, M. Arnaud, M. Ashdown et al., *Planck 2015 results. XXVI. The Second Planck Catalogue of Compact Sources*, *A&A* **594** (2016) A26 [1507.02058].
- [71] M. Tristram, J. F. Macías-Pérez, C. Renault and D. Santos, *XSPECT, estimation of the angular power spectrum by computing cross-power spectra with analytical error bars*, *MNRAS* **358** (2005) 833 [astro-ph/0405575].
- [72] Planck 2018 results. III., *Planck 2018 results. III. High Frequency Instrument data processing and frequency maps*, *A&A* **641** (2020) A3 [1807.06207].
- [73] T. L. Makinen, A. Heavens, N. Porqueres, T. Charnock, A. Lapel and B. D. Wandelt, *Hybrid summary statistics: neural weak lensing inference beyond the power spectrum*, *arXiv e-prints* (2024) arXiv:2407.18909 [2407.18909].